A Silanol-Functionalized Polyoxometalate with Excellent Electron Transfer Mediating Behavior to ZnO and TiO_2 Cathode Interlayers for Highly Efficient and Extremely Stable Polymer Solar Cells

Marinos Tountas,[a,b] Yasemin Topal,[c] Apostolis Verykios,[a,d] Anastasia Soultati,[a] Andreas Kaltzoglou,[a] Theodoros A. Papadopoulos,[e] Florian Auras,[f] Kostas Seintis,[d] Mihalis Fakis,[d] Leonidas C. Palilis,[d] Dimitris Tsikritzis,[g] Stella Kennou,[g] Azhar Fakharuddin,[h] Lukas Schmidt-Mende,[h] Spyros Gardelis,[i] Mahmut Kus,[c] Polycarpos Falaras,[a] Dimitris Davazoglou,[a] Panagiotis Argitis,[a] Maria Vasilopoulou[a,*]

Combining high efficiency and long lifetime under ambient conditions still poses a major challenge towards commercialization of polymer solar cells. Here we report a facile strategy that can simultaneously enhance the efficiency and temporal stability of inverted photovoltaic architectures. Inclusion of a silanol-functionalized organic-inorganic hybrid polyoxometalate derived from PW_9O_{34} lacunary phosphotungstate anion, namely $(nBu4N)_3$ $[PW_9O_{34}(tBuSiOH)_3]$, significantly increases the effectiveness of the electron collecting interface, which consists of a metal oxide such as titanium dioxide or zinc oxide, and leads to a high efficiency of 6.51% for single-junction structures comprising of poly(3-hexylthiophene):indene-C60 bisadduct (P3HT:$IC_{60}BA$) blends. The above favourable outcome stems from a large decrease in the work function, an effective surface passivation and a decrease in surface energy of metal oxides which synergistically result in the outstanding electron transfer mediating capability of the functionalized polyoxometalate. In addition, the insertion of silanol-functionalized polyoxometalate layer significantly enhances the temporal stability of unencapsulated devices by retaining nearly 90% of their original efficiencies (T_{90}) after 1000 hours of exposure in ambient environment.

Introduction

The development of highly efficient, environmentally friendly alternative technologies for solar-energy conversion at low cost is essential due to the unprecedented growth in energy usage in recent years. Polymer solar cells (PSCs) have attracted growing attention over the past decades because of their advantages in fabricating low cost, lightweight, flexible and large size light harvesting devices.[1-3] For an optimized use of solar energy, however, efficient as well as stable PSCs are required. Since the first report on organic bulk heterojunction (BHJ) solar cells, substantial progress has been made resulting in device efficiencies above 10%.[4,5] Aside from improvements in the design and synthesis of active materials,[6-8] interface engineering, which usually comprises the insertion of appropriate transport interlayers, has emerged as key factor for boosting PSCs efficiency and stability.[9-13] Metal oxide-based semiconductors, in particular, zinc oxide (ZnO) and titanium dioxide (TiO_2), have been recognized as efficient cathode interlayers (CILs) in PSCs due to their excellent optical transparency, low-toxicity and solution-based fabrication.[14-16] However, there are limitations in using as-deposited ZnO and TiO_2 firstly due to their moderate n-type conductivity, especially in the case of TiO_2, and secondly due to high recombination rates of photogenerated electron-hole pairs at surface trap states of metal oxides. Both effects hamper the efficiency of electron transfer towards the cathode contact.[17-20] In addition, the relatively high work function (W_F) of ZnO and TiO_2 may lead to a significant electron extraction barrier at the metal oxide/organic interface. Furthermore the lack of compatibility between hydrophilic metal oxides and hydrophobic polymers usually causes non-optimal surface coverage and macroscopic phase separation. All these result in inferior device performance and poor overall stability.

To overcome these limitations several strategies have been developed such as the implementation of appropriate surface modifiers, usually polyelectrolytes with acidic and amino groups,[21-23] self-assembled monolayers (SAMs)[24-26] and organic nano-dots,[27-29] which optimize the W_F of the interlayers as well as the contact between the interlayers and the photoactive blend. However, these organic modifiers suffer from insulating properties, thus limiting the device efficiency. On the contrary, doping of metal oxides with several elements,[30-34] and appropriate gas treatment,[35,36] have simultaneously increased their conductivity and passivated surface defects thus accelerating electron transfer towards cathode extending their effectiveness as CILs in PSCs. Polyoxometalates (POMs), which represent a large family of environmentally friendly inorganic clusters, are promising candidates for multi-electron transfer catalysts, as they are stable against oxidative degradation and can receive a large number of electrons without deforming their structures.[37,38] They were recently used by our group and others as cathode interlayers in PSCs with either the conventional or the inverted architecture due to their unique properties, such as facile processing from water or alcohol solutions, adequate electron mobility, and high transparency in the visible range.[39-44] However, their possible aggregation when forming a solid film from aqueous solutions may be extremely harmful to device performance and stability; consequently, it is rather unlikely for pristine POMs to be suitable for large-area production of PSCs. As yet, works to exploit appropriate concepts to simultaneously achieve superior electron transfer

properties of POMs while also avoiding aggregation for successful application in PSCs are limited.[43,44]

In order to overcome these drawbacks and utilize the unique advantages of POMs we synthesized a silanol functionalized POM-based complex containing the PW_9O_{34} POM cluster with the lacunary Keggin structure namely $(nBu4N)_3$ $[PW_9O_{34}(tBuSiOH)_3]$ (chemical formula $C_{61}H_{139.5}N_{3.5}PO_{37}Si_3W_9$) (referred to as tBuSiOH-POM), which is inserted into the vicinity of the metal oxide/organic interface to allow superior electron transfer to TiO_2 and ZnO CILs. The effective anchoring of tBuSiOH-POM onto metal oxide substrates through silanol linkers results in the formation of a uniform POM film. The insertion of such film into the device structure simultaneously offers a large work function decrease and an effective surface passivation of metal oxides increasing the device open-circuit voltage (V_{oc}). The presence of hydrophobic tertiary butyl groups,[45,46] decreases the surface energy of the substrate resulting in the formation of homogeneous and closely packed photoactive films improving the device fill factor (FF). The outstanding electron transfer mediating capability of POM to metal oxides induces a large enhancement in the short-circuit current (J_{sc}). Consequently, when a tBuSiOH-POM film is applied as the electron transfer mediator between the photoactive film, composed of a poly(3-hexylthiophene):indene-C60 bisadduct (P3HT:$IC_{60}BA$) blend, and the metal oxide, power conversion efficiencies (PCEs) of up to 6.51% were observed. Besides we observed a remarkable temporal stability of intentionally unencapsulated cells which preserve more than 90% of their initial PCE (T_{90}) after 1000 h of exposure in ambient environment. Improved device performance was also obtained when using P3HT:[6,6]-phenyl-C71butyric acid methyl ester)($PC_{71}BM$) and (poly[[4,8-bis[(2-ethylhexyl)oxy]benzo[1,2-b:4,5-b']dithiophene-2,6-diyl][3-fluoro-2-[(2-ethylhexyl) carbonyl] thieno[3,4-b] thiophenediyl]](PTB7):$PC_{71}BM$ as the photoactive blends while indium tin oxide (ITO) modified with tBuSiOH-POM worked effectively as cathode contact demonstrating the universality of our approach.

Experimental

Synthesis of lacunary POM materials. Details on the synthesis of α-$K_9[PW_9O_{34}]\cdot 16H_2O$ were given elsewhere.[44] To a well stirred suspension of α-$K_9[PW_9O_{34}]\cdot 16H_2O$ (10g, 3.48 mmol) in dry MeCN (200 mL) under argon solid nBu_4NBr (6 g A, 18.6 mmol) were added and then $tBuSiCl_3$ (2.1 g, 10.1 mmol) the mixture was stirred overnight at 0˚C. After separation of the white solid (KCl+KBr), white crystals of $(nBu_4N)_3[PW_9O_{34}(tBuSiOH)_3]$ formed upon slow evaporation of the resulting solution in an open vessel at room temperature.[47]

Titanium dioxide layer preparation. FTO-coated glass (Pilkington TEC 15, <15 Ohms/sq) was cleaned by sonication in detergent solution (Hellmanex III, Hellma Analytics), water and ethanol, followed by treatment in an oxygen plasma for 5 min. A solution of 13 µL concentrated aqueous HCl in 5 mL of isopropanol was slowly added to a stirred solution of titanium isopropoxide (711 mg, 2.5 mmol) in 5 mL of dry isopropanol. The cleaned substrates were spin-coated at 2000 rpm with this titania precursor solution and immediately placed on a hotplate at 150 °C. Subsequently, the samples were calcinated in air at 500 °C for 45 min (1 h ramp).

Zinc oxide layer preparation. A 0.5 M ZnO sol-gel was prepared using zinc acetate dehydrate (Sigma Aldrich) in ethanolamine and 2-methoxyethanol. The mixture was stirred until completely dissolved and was subsequently filtered using a PVDF 0.45 mm filter. Fluorine doped tin oxide conducting substrates (FTO) from Solaronix (TCO10-10) were sequentially cleaned ultrasonically with soap water, distilled water, acetone and isopropanol. The substrates were introduced into an oxygen plasma chamber for 7 min prior to ZnO coating. The ZnO films were prepared from a two-step spin coating procedure as follows: An amount of ZnO sol-gel to was poured onto the substrate to fully cover it and was spin coated at 6000 rpm (acceleration 6000 rpm for 40 sec). The films were immediately put on a pre-heated hot-plate at 80 °C. The substrates were annealed at 250 °C for 10 min. Once cooled down to 60 °C, the same procedure is repeated.

Device Fabrication. Polymer solar cells were fabricated on 50 nm thick ZnO and TiO_2 films on FTO substrates. Then a tBuSiOH-POM film was deposited via spin coating a 5 mg ml^{-1} solution in acetonitrile at 1000 rpm for 40 sec. P3HT:$IC_{60}BA$ blends were spin coated inside an argon filled glove box at 800 rpm for 30 sec from solution consisting of 17 mg ml^{-1} P3HT and 17 mg ml^{-1} $IC_{60}BA$ (P3HT was purchased from Rieke metals and $IC_{60}BA$ was purchased from Ossila) in 1.2 dichlorobenzene and left to dry before for 30 min before heating at 150 °C for 10 min. Then, an approximately 20 nm-thick under-stoichiometric molybdenum oxide (MoO_x) layer was deposited on top of the active layer to serve as the hole extraction layer. The devices were completed with a 150 nm thick aluminium anode, deposited in a dedicated thermal evaporator at a pressure of 10^{-6} Torr through a shadow-mask, which defined the device active area to be equal to 12.56 mm^2.

Measurements and Instrumentation. X-ray photoelectron spectra (XPS) and ultraviolet photoelectron spectra (UPS) were recorded by Leybold EA-11 electron analyzer operating in constant energy mode at pass energy of 100 eV and at a constant retard ratio of 4 eV for XPS and UPS respectively. All binding energies were referred to the C 1s peak at 284.8 eV of surface adventitious carbon, respectively. The X-ray source for all measurements was an unmonochromatized MgKα line at 1253.6 eV (12 keV with 20 mA anode current). The valence band spectra of titanium and zinc oxide without and with tBuSiOH-POM were evaluated after recording the UPS spectra of metal oxide/POM films deposited on an FTO substrate. For the UPS measurements, the He I (21.22 eV) excitation line was used. A negative bias of 12.22 V was applied to the samples during UPS measurements in order to separate secondary electrons originating from sample and spectrometer and to estimate the absolute work function value from the high BE cut-off region of the UPS spectra. The analyzer resolution is determined from the width of the Au Fermi edge to be 0.16 eV. The steady-state photoluminescence spectra of P3HT on various substrates were taken by means of a Fluoromax spectrometer (Horiba) upon excitation at 550 nm. The films were placed on a specific holder for solid samples and the spectra were

corrected for the sensitivity of the detector. The PL dynamics of the samples were studied under magic angle conditions, by using a femtosecond upconversion technique. The excitation of the samples was realized by means of the second harmonic of a Ti:Sapphire laser at 410 nm. The average power was less than 3 mW while the repetition frequency was 80 MHz. The PL of the samples was collected and focused together with the remaining fundamental fs laser beam on a 0.5 mm BBO crystal to produce frequency mixing. The upconverted beam passed through an iris, filters and a monochromator and was detected by a photomultiplier. The Instrument's Response Function (IRF) was approximately 150 fs. A three-exponential function convoluted with the IRF was used for fitting the dynamics. Absorption, transmittance and reflectance measurements were taken using a Perkin Elmer Lambda 40 UV/Vis spectrophotometer. The thicknesses of films were measured with an Ambios XP-2 profilometer or a M2000 Woolam ellipsometer. The surface morphology of films was analyzed with an NT-MDT atomic force microscope (AFM) operating in semicontact mode with the frequency set at 1 Hz. Current density-voltage characteristics of the fabricated solar cells were measured with a Keithley 2400 source-measure unit. Cells were illuminated with a Xe lamp and an AM 1.5G filter to simulate solar light illumination conditions with an intensity of 100 mW/cm^2 (1 sun), as was recorded with a calibrated silicon photodiode. EQE measurements were carried out using an Autolab PGSTAT-30 potentiostat, with a 300 W Xe lamp in combination with an Oriel 1/8 monochromator for dispersing the light in an area of 0.5 cm^2. A Thorlabs silicon photodiode was used for the calibration of the spectra. All measurements were performed in air.

Computational Methodology. Spin-polarized calculations for the isolated tBuSiOH-POM were performed using the Vienna Ab Initio Simulation Package (VASP). Plane-wave basis sets and the Perdew-Burke-Ernzerhof (PBE) functional was used along with the Grimme DFT-D2 method, taking into account spin-orbit coupling. Geometry optimization was carried out with maximum atomic forces set at 0.01 e·Å^{-1}; initial atomic coordinates of the molecular structure were taken from work done by Zhang et al.[48] The Density of States (DOS) was extracted via the projector augmented wave (PAW) method, with a plane-wave cut-off energy of 400 eV and a Γ centered k-point grid of 2×2×2. Gaussian smearing with a width of 0.05 eV was used to determine how partial occupancies are set for each wave-function. Finally, the POM supercell was modeled within a simple cubic cell of dimensions a=20 Å.

Results and discussion

Efficiency and stability enhancement of PSCs using tBuSiOH-POM. A simple, and low-cost synthetic procedure of tBuSiOH-POM providing high-yield is given in the experimental section. In general, starting from the trivacant highly-charged tungstophosphate $[PW_9O_{34}]^{7-}$, it has been possible to graft directly tertiary butyl (tBu)-silane moieties and an "open-structure" derivative was obtained which keeps its trifold rotational symmetry. The detailed material characterization in solution, using FTIR, UV-vis, ^{31}PNMR, ^{1}HNMR spectroscopies and cyclic voltammetry, is presented in the Supporting Information (Figures S1-S3). Notably, the lowest unoccupied molecular orbital (LUMO) of the functionalized POM was calculated at -4.38 eV (Fig. S3) and is well aligned to the bottom of the conduction band (CB) of TiO_2 and ZnO,[49] while its highest occupied molecular orbital (HOMO) is placed at -8.32 eV indicating excellent hole blocking capability of the material. The coverage of TiO_2 and ZnO with POM film was monitored using X-ray photoelectron spectroscopy (XPS) of the TiO_2/tBuSiOH-POM and ZnO/tBuSiOH-POM interfaces (Figures S4, S5) which clearly shows the W4f peaks of PW_9O_{34} parent compound and the Si2p and N1s of the functional groups confirming that the functionalized POM is present on the metal oxide surfaces. In addition, the XPS peaks reveal a significant degree of reduction (understoichiometry) of POM on metal oxides, as concluded from the appearance apart from the well-defined doublet, characteristic of the W^{6+} states, of a peak at lower BEs which is attributed to lower (W^{5+}) oxidation states of the WO_3 units. The reduction of POMs has previously been considered to be the origin of improved electron transport and increased electron mobility of those materials.[44]

The effect of a tBuSiOH-POM film spin-coated on metal oxides from a solution in acetonitrile, on the device performance was evaluated in PSCs using the device architecture of FTO/CIL/tBuSiOH-POM/P3HT:$IC_{60}BA$/MoO_x/Al where the CIL was either TiO_2 or ZnO (Figure 1a). In addition, PSCs without tBuSiOH-POM were used as the reference devices. The chemical structures of organic semiconductors used in this study and of tBuSiOH-POM are shown in Figure 1b, where the anchoring of the functionalized POM on TiO_2 or ZnO surface via silanol linker groups is also illustrated.[46] The transmittance spectra of TiO_2 and ZnO films on glass substrates before and after coverage with POM film are shown in Figure 1c. A small increase of the transmittance of metal oxide layers upon POM coating is observed, which is beneficial for the device performance since more light passes through the FTO/metal oxide/POM interfaces to be absorbed from the photoactive blend. Note that the absorption spectra and bandgap of TiO_2 and ZnO films remained unaffected upon POM deposition (Figures S6, S7).

Figure 1d presents the current density–voltage (J–V) characteristics of the above four kinds of devices under 1 sun (100 mW cm^{-2}) illumination using a AM 1.5G filter. The corresponding dark J-V curves are shown in Figure 1e. Table 1 presents the overall photovoltaic performance of the devices. Compared to the reference devices, those with the tBuSiOH-POM resulted in a simultaneous enhancement in V_{oc}, J_{sc} and FF irrespective of the metal oxide interlayer. Specifically, for the TiO_2 based devices J_{sc} increased from 9.58 mA cm^{-2} to 10.66 mA cm^{-2}, V_{oc} from 0.78 V to 0.83 V and FF from 0.63 to 0.73 thus boosting the PCE from 4.71% to 6.46%; the latter represents a 37% enhancement as compared to the reference cell. Similarly, the PCE of the ZnO based device was increased from 5.03% to 6.51%, which, to the authors knowledge, is among the highest efficiencies obtained in PSCs based on the P3HT:$IC_{60}BA$ system,[50] which is usually selected as the front cell active material in tandem PSCs.[5] In this context, the devices using the ZnO CIL were always slightly over performing as compared to their counterparts based on TiO_2 probably due to the higher transparency and n-type conductivity of ZnO.[51] The increase in the FF and the carrier collection efficiency are related to the significant decrease of the series resistance, R_s, and the large increase of the shunt resistance, R_{sh}, (Table 1) which indicate an overall enhanced quality of the cathode contact of the POM-modified devices. Additionally, the observed increase in V_{oc} could be ascribed to the suppression of the dark reverse saturation current which is correlated with the enhanced built-in voltage of the modified devices, as evidenced by the dark J-V characteristics (Fig. 1e). In the devices with as-deposited TiO_2 or ZnO CILs, the low built-in field results in higher carrier accumulation and recombination inside the cell, thus leading to large dark reverse saturation current.[52,53] When tBuSiOH-POM is embedded at the cathode interface, the built-in field is largely increased suggesting a suppression

in carrier accumulation and recombination, as also evident from decreased reverse saturation current.

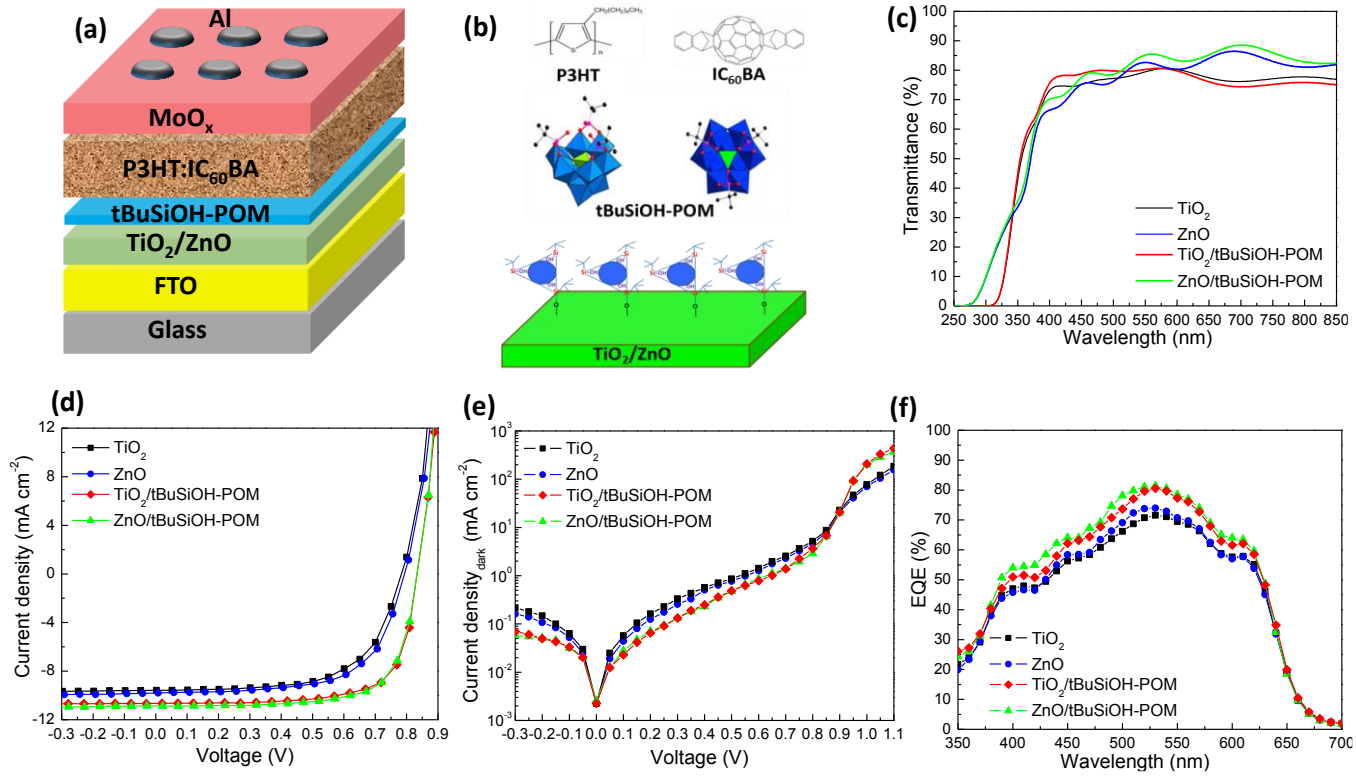

Figure 1 (a) The inverted PSC architecture used in this study. (b) The chemical structures of the organic semiconductors used in the photo-active layer of PSC devices (up) and the polyhedral representation of tBuSiOH-POM where WO_6 octahedra appear in blue color, PO_4 tetra-hedron appears in green color, and Si, C and O appear in pink, black and red color, respectively (middle). Coordination of tBuSiOH-POM to TiO_2 or ZnO substrate via the formation of Si-O-Ti/Zn bonds (bottom). (c) Transmittance spectra of as-deposited and tBuSiOH-POM coated TiO_2 and ZnO films on glass/FTO substrates. (d) J-V characteristics under 1.5 AM illumination of P3HT:IC_{60}BA-based devices fabricated on FTO/TiO_2 or FTO/ZnO substrates without and with tBuSiOH-POM. (e) The dark J-V characteristics and (f) the EQE spectra of PSCs without and with tBuSiOH-POM.

Table 1. Device characteristics of polymer solar cells having the device configuration FTO/TiO_2 or ZnO/tBuSiOH-POM/P3HT:IC_{60}BA/MoO_x/Al (mean values and standard deviations were extracted from a batch of 20 independent devices).

CIL	J_{sc} (mA cm^{-2})	$J_{sc(EQE)}$ (mA cm^{-2})	V_{oc} (V)	FF	PCE (%)	R_s (Ω cm^2)	R_{sh} (Ω cm^2)
TiO_2	9.58 (±0.15)	9.68	0.78 (±0.01)	0.63 (±0.01)	4.71 (±0.13)	4.9	3821
ZnO	9.80 (±0.09)	9.81	0.79 (±0.01)	0.65 (±0.01)	5.03 (±0.11)	3.8	2557
TiO_2/tBuSiOH-POM	10.66 (±0.14)	10.62	0.83 (±0.01)	0.73 (±0.01)	6.46 (±0.09)	1.6	6586
ZnO/ tBuSiOH-POM	10.89 (±0.10)	10.86	0.83 (±0.01)	0.72 (±0.01)	6.51 (±0.10)	1.4	6297

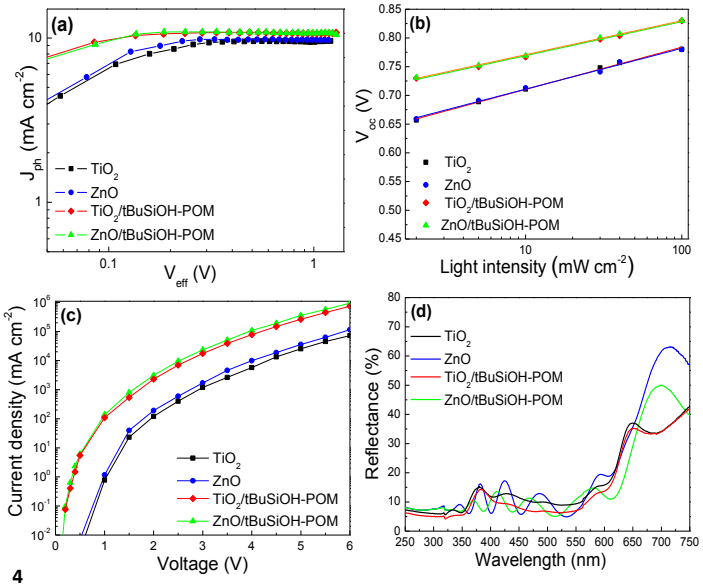

Figure 2 (a) Net photocurrent density and (b) dependence of V_{oc} on 1.5 AM illuminated light intensity of P3HT:IC_{60}BA-based devices fabricated on FTO/TiO_2 or FTO/ZnO substrates without and with tBuSiOH-POM. (c) Current density-voltage (J–V) curves (measured in dark) in semi-log plot of electron-only devices with the structure: FTO/TiO_2 or ZnO without and with tBuSiOH-POM/P3HT:IC_{60}BA/Al. (d) Reflectance spectra of the complete PSC devices.

The enhancement in J_{sc} can be associated with a more effective photon-to-electron conversion efficiency in the POM-modified de-vices as shown in Figure 1f where the corresponding external quan-

tum efficiency (EQE) spectra of the devices before and after the insertion of POM are presented. The EQE values of the POM-modified PSCs are significantly higher in the wavelength range of 450–650 nm (which is the absorption range of P3HT) than those of the reference devices, which is consistent with the tendency of J_{sc} of the PSCs based on different CILs. In addition, the EQE spectra of the devices were integrated from 300 to 800 nm and $J_{sc(EQE)}$ values were calculated from the integration and listed in Table 1. Notably, these values are very consistent with the J_{sc} obtained from J–V characteristics under illumination indicating the reliability of the measured J_{sc}.[54,55]

The better performance of the devices with tBuSiOH-POM was also supported by the dependence of the photocurrent density (J_{ph}) on the effective voltage (V_{eff}), where J_{ph} equals to J_L-J_D (J_L and J_D are the current density under 1.5 AM illumination and dark conditions, respectively) and V_{eff} equals to V_0 -V (V_0 is the voltage at J_{ph}=0 and V is the applied voltage).[56,57] From Figure 2a it becomes evident that J_{ph} is larger and reaches saturation (J_{sat}) at smaller effective voltage for both kinds of POM embedding devices as compared to the reference ones. This indicates that incorporation of tBuSiOH-POM into the device facilitates excitons dissociation into free carriers, and both the exciton generation rate and the dissociation probability were increased, thereby enhancing the photocurrent of PSCs. In particular, taking into account that the $J_{ph}/J_{ph,sat}$ ratio is related to exciton dissociation and charge collection probabilities, we found that under short-circuit conditions, the reference devices based on TiO_2 and ZnO give $J_{ph,sc}/J_{ph,sat}$ ratios of 92.1% and 93.0%, respectively. The $J_{ph,sc}/J_{ph,sat}$ ratios of the corresponding PSCs with tBuSiOH-POM are 97.0% and 97.5%, respectively which clearly implies that the PSCs with POM exhibit better exciton dissociation and enhanced charge extraction and collection. Accordingly, we infer that the best photovoltaic performance of the functionalized POM PSCs originates from enhanced exciton dissociation but also from reduced bimolecular recombination. The reduced bimolecular recombination losses of the POM-modified cells were further probed by measuring the dependence of V_{oc} on the illuminated light intensity, as shown in Figure 2b, where the log-linear plots of V_{oc} as a function of the light intensity are presented. The slope values of V_{oc} were decreased significantly from 1.24 and 1.20 k_BT/q to 1.02 and 1.01 k_BT/q upon POM insertion into the TiO_2 and ZnO-based cells, respectively, where k_B is Boltzmann's constant, T is the absolute temperature, and q is the elementary charge. The relatively large slopes of the reference devices indicate an increased number of trap assisted Shockley-Read-Hall monomolecular recombination losses.[58-60] The decreased slopes of POM embedding devices indicate much lower trap assisted recombination at open circuit and an enhancement of cathode selectivity. They also imply that the insertion of POM into the vicinity of the cathode interface effectively improves the charge transport ability as also evidenced by the J-V curves of electron-only devices shown in Figure 2c. This improvement in electron current density can be related to a decrease of the electron extraction barrier upon tBuSiOH-POM insertion. The enhanced electron current is believed to contribute to the improved J_{sc} in the PSCs with the functionalized POM. The higher absorption of the POM-modified cells also contributes to the enhancement in J_{sc}. As shown in Figure 2d, where the reflectance spectra of the complete PSCs under study are presented, the lower reflectivity of the POM-modified devices in the whole spectrum indicates stronger absorption of the incident light.

Thereafter, we monitored the stability of the four kinds of PSCs as a function of storage time in air. The PSC devices for shelf time stability tests were intentionally unencapsulated, stored in dark inside a nitrogen filled desiccator between measurements, and measured under ambient condition (temperature 20-25 ^oC and relative humidity of 25-40%). As shown in Figure 3d, in terms of the PCEs of typical reference devices based on metal oxide CILs they decreased to 90% of their initial values (T_{90}) to about three days while they diminished to 50% (T_{50}) after less than a month. In striking contrast, the typical devices using tBuSiOH-POM coated metal oxide CILs demonstrated superior stability and maintained more than 90% of the original device PCE (T_{90}) after 1000 h of operation in ambient air.

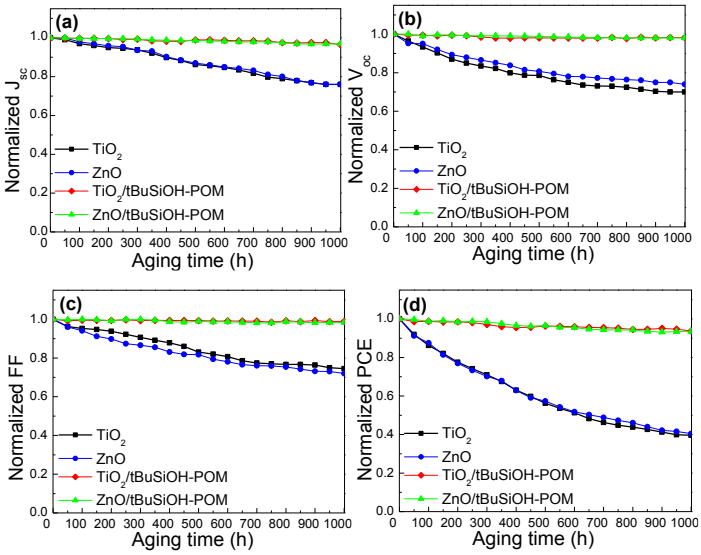

Figure 3 Stability measurements in ambient air: Variation (as derived from measurements on 5 individual devices of each kind) of normalized (a) J_{sc}, (b) V_{oc}, (c) FF and (d) PCE, over a period of 1000 hours for P3HT:$IC_{60}BA$-based devices using TiO_2 and ZnO without and with tBuSiOH-POM.

The variation of key photovoltaic performance parameters versus storage time is presented in Figures 3a-c. Such exceptional temporal stability can be attributed to the functionalized POM, which forms an internal passivation layer on metal oxide CILs. It is well known that surface defects of TiO_2 and ZnO act as binding sites for the adsorption of oxygen and water molecules, which are detrimental to the ambient stability of the devices. We speculate that the anchoring of tBuSiOH-POM on the metal oxide surface via the formation of strong Si-O bonds, induces effective surface passivation thus preventing the formation of oxygen-induced trap states,[61,62] while also prevents access of water to the metal oxide/photoactive layer interface. In addition, the tertiary butyl hydrophobic component of POM forms an internal stable hydrophobic

encapsulating layer of the organic film retarding the degradation of both electrodes and photoactive materials, leading to more stable devices.

Surface properties of metal oxide/tBuSiOH-POM CILs. The dependence of solar cell performance parameters on tBuSiOH-POM suggests that more details need to be known about the morphology of the deposited films so as to investigate how such factor may contribute to the improved device performance. Atomic force microscopy (AFM) was used to monitor the surface morphology of TiO_2 and ZnO before (Figures 4a and c) and after coverage with tBuSiOH-POM (Figures 4b and d). A TiO_2 and ZnO film (~50 nm) is deposited on FTO with a root mean square (RMS) roughness of 3.2 and 5.7 nm, respectively. After the insertion of POM layer (which was estimated ~5 nm in the case of TiO_2 while was rather thinner in the case of ZnO probably because it follows the nanostructured nature of the latter) on metal oxides their surfaces are smoother with RMS roughness of 2.5 and 4.9 nm, respectively. The physical contact between metal oxide and photoactive blend might be enhanced by a decrease in surface roughness. Another critical parameter, the surface energy, can have its own impact on the investigated system. In the case of PSCs, the surface energy can play a significant role in the formation of the morphology by directing the phase-separation process during deposition. Surface modification of metal oxides with tBuSiOH-POM can change their wettability and thus the surface energy altering the way in which the subsequently deposited organic photoactive blend assembles and orients itself on the surface. Changes in wettability were confirmed by measuring the contact angle of water and calculating surface energy (Figures S8, S9 and Table S1) of the different substrates. The as-deposited TiO_2 and ZnO substrates are rather hydrophilic showing relatively low water contact angles of 45.0° and 46.7°, respectively, and high surface energies of 58.74 and 59.47 mJ m^{-2} whereas water contact angles of 52.1° and 54.2° and surface energies of 52.62 and 53.93 mJ m^{-2} were measured for the POM-coated TiO_2 and ZnO substrates, respectively. It has been previously suggested that, as the hydrophilicity and surface energy of metal oxide layer are reduced to a moderate value (around 50 mJ m^{-2}),[63] its interfacial contact with photoactive blend is enhanced. The tertiary butyl (tBu)-silane group was selected as the hydrophobic component of the functionalized POM in order to adjust its wetting properties and achieve desirable surface energies,[64] to guarantee sufficient hydrophobicity and to enable better adhesion of the photoactive overlayer. The nanomorphology of photoactive blend on TiO_2 and ZnO films without (Figures 4e and g) and with tBuSiOH-POM (Figures 4f and h) was studied with AFM. 2D 5x5 μm^2 topography images of P3HT:$IC_{60}BA$ spin-coated on as-deposited and POM-coated metal oxide substrates reveal that the distribution of P3HT donor and $IC_{60}BA$ acceptor and their interpenetrating networks are quite different. In particular, smaller donor:acceptor domains, an indication of finer, smaller scale phase separation, are formed when photoactive blends are deposited on POM-coated TiO_2 and ZnO. In addition, a significant reduction in the RMS roughness of the blend deposited on POM-modified TiO_2 (8.35 nm) and ZnO (8.22 nm) as compared to the blends deposited on as-deposited TiO_2 (16.55 nm) and ZnO (14.63 nm) is observed. The above results indicate that the film formation and physical contact at the metal oxide/tBuSiOH-POM/photoactive layer interfaces are more uniform and should lead to better electrical contact, which are beneficial to the exciton charge separation and charge transport.

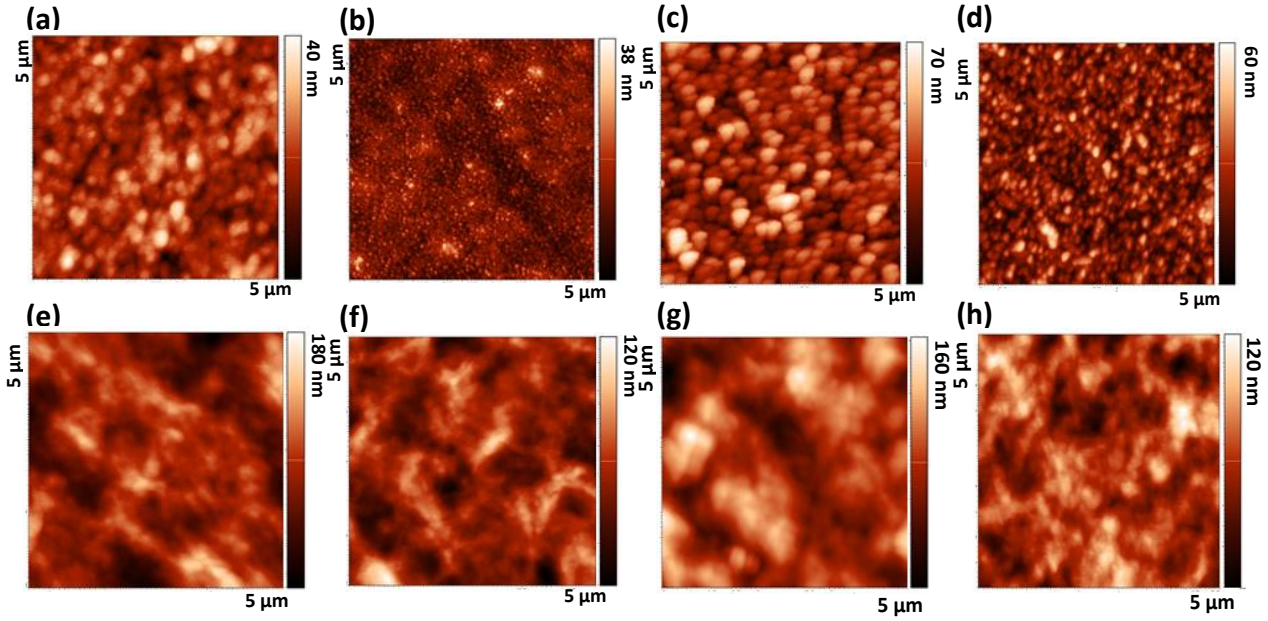

Figure 4 2D 5x5 μm^2 AFM topography of (a) as-deposited TiO_2 and (b) tBuSiOH-POM coated TiO_2 films, of (c) as-deposited ZnO and (d) tBuSiOH-POM coated ZnO films. 2D AFM surface topography (5x5μm^2) of P3HT:$IC_{60}BA$ films deposited on (e) TiO_2 and (f) tBuSiOH-POM coated TiO_2 films, on (g) ZnO and (h) tBuSiOH-POM coated ZnO films.

tBuSiOH-POM-induced changes in metal oxides W_F. The primary requirement of cathode interlayers lies in their ability to lower the W_F of the electrode by producing large interfacial dipoles that induce a downward vacuum-level shift. To test this in the case of tBuSiOH-POM modified metal oxides, ultraviolet photoelectron spectroscopy (UPS) was used to probe the electronic properties of TiO_2 (Figure 5a) and ZnO (Figure 5b) before and after POM coverage. It is observed that, upon deposition of a thin POM layer, the cut-off region of the UPS spectra shifted towards higher binding energy, indicating a reduction in the magnitude of the W_F of TiO_2 and ZnO. In particular, the W_F of TiO_2 (4.4 eV) is shifted to 3.6 eV and that of ZnO (4.5 eV) is shifted to 3.7 eV upon POM coverage. The W_F change (ΔW_F) is 0.8 eV in both cases. Such a significant W_F change can be probably attributed to the polar nature of the terminal –OH groups of the functionalized POM. Figure S10 shows the near Fermi level region of the TiO_2/tBuSiOH-POM interface in more detail; the spectrum exhibits an extra emission peak at 1.5 eV. This peak can be attributed to photoelectrons coming from the LUMO of tBuSiOH-POM which is filled upon electron transfer from trap states of TiO_2 lying just below the CB of the latter. Such electron transfer results firstly on the effective surface passivation of TiO_2 and secondly on the reduction and, therefore, the increase electron conductivity of the functionalized POM.[40] Both are beneficial for the device performance.

The decreased W_F of POM/metal oxide cathodes can also increase the built-in field used to break the electrical symmetry inside of the cells which is beneficial to charge extraction efficiency. The reduction in W_F associated with the tBuSiOH-POM dipole layer is illustrated in the energy band of the cathode interfaces presented in Figures 5c and d. It is observed that upon POM coverage of metal oxides their W_F is significantly reduced by 0.8 eV which implies that the vacuum level shifts through the formation of an interfacial large dipole with the negative pole pointing away from the POM-modified oxide surface (Figure 5d). This implies that the band offset for electron transfer from the $IC_{60}BA$ LUMO to the conduction band of metal oxides decreases thus providing barrier-free electron transport under short-circuit conditions and further enhances the built in field, thus facilitating charge extraction. Note that, the low W_F values of tBuSiOH-POM/metal oxide electrodes allow them to form better contacts not only with P3HT:$IC_{60}BA$ blend but also with the P3HT:$PC_{71}BM$ and PTB7:$PC_{71}BM$ ones, as can be concluded from the performance enhancement obtained in POM modified devices using those blends as the photoactive layers.

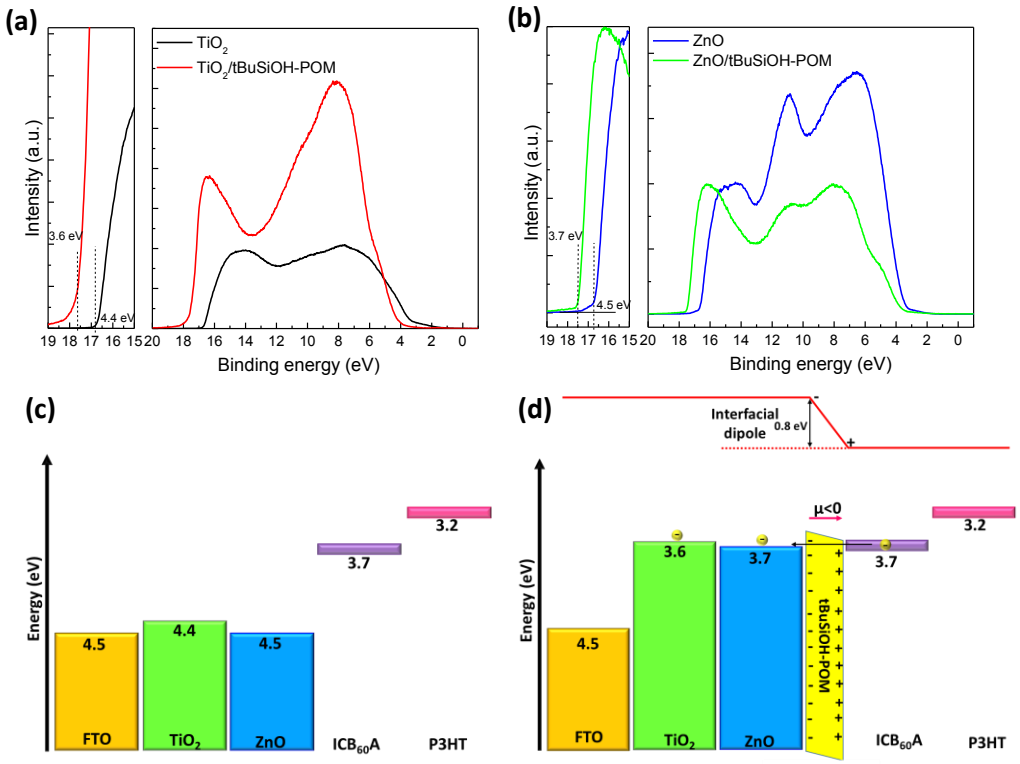

Figure 5 UPS measurements of (a) as-deposited and tBuSiOH-POM coated TiO_2 and (b) as-deposited and tBuSiOH-POM coated ZnO films. (c) Energy level alignment at various cathode interfaces of the inverted devices considering vacuum level alignment. (d) Illustration of the formation of a negative interfacial dipole at the metal oxide/tBuSiOH-POM/$IC_{60}BA$ interface.

In particular, the PCE of P3HT:$PC_{71}BM$-based devices increased from 3.17% (for the reference device using TiO_2) and 3.41% (for the reference device using ZnO) to 4.41% and 4.42%, respectively, upon POM coverage of metal oxides (Figure S11 and Table S2). Similarly, the PCE of PTB7:$PC_{71}BM$-based devices increased from 6.37% and 6.65% to 8.11% and 8.37%, upon POM coverage of TiO_2 and ZnO, respectively (Figure S12 and Table S3). Notably, the deposition of tBuSiOH-POM directly on ITO substrates remarkably enhanced the electron selective

capability of the latter as demonstrated from the significant efficiency enhancement of PSCs with the structure ITO/tBuSiOH-POM/P3HT:$IC_{60}BA$/MoO_3/Al up to 4.58% which represents a huge enhancement as compared to 0.29% of the reference cells without POM (Figure S13 and Table S4). This result obviates that tBuSiOH-POM except of electron transfer mediator to TiO_2 and ZnO CILs can be also used as efficient electron transport interlayer directly deposited to cathode electrodes; however, further investigation is needed.

Theoretical investigation of tBuSiOH-POM induced surface passivation of metal oxides. In order to further explore the effect of surface passivation due to electron transfer between the oxide surfaces and POM adsorbate, as indicated previously via UPS measurements, the electronic structure of the latter was studied via density functional theory (DFT) following the procedure described in the methodology section. After optimizing the molecular structure of the isolated compound (Figure S14), the total density of states as well as the projected density of states from individual atom contributions were extracted and plotted in Figure 6. It is observed that the valence band maximum (VBM) is located at -0.1 eV below the Fermi level (0 eV) and consists of O 2*p*, C 2*p*, and H 1*s* orbitals with a mild hybridization from Si 3*p* and W 5*d* orbitals. It is interesting to see that the DOS also shows a sharp peak of unoccupied states in the middle of the band gap, which is contributed primarily by H 1*s*, C 2*p* and Si 3*p* orbitals with minimal hybridization from O 2*p* and W 5*d* orbitals. The location of this peak indicates that effective energy level alignment at the interface between the metal-oxide surface and POM may favor electron transfer from metal-oxide surface trap states to POM adsorbate. The latter would provide a route for metal-oxide surface passivation and instigate a downward vacuum-level shift causing the reduction of the POM-modified surface work function of the metal oxides as observed experimentally.

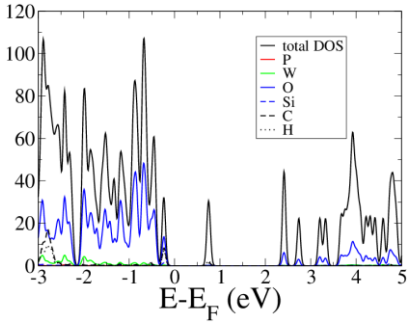

Figure 6 Total density of states of the isolated tBuSiOH-POM compound as well as individual contributions from its constituent atoms. The Fermi level is located at 0 eV.

Electron transfer mediating capability of tBuSiOH-POM. A key motivation for this work is to see if the metal oxide/organic interface can be affected by the electron shuttling efficiency of POM. To investigate the electron transfer mediating capability of tBuSiOH-POM from the photoactive to metal oxides we monitored the photoluminescence of P3HT films on TiO_2 and ZnO before and after POM coverage. Note that we used pristine P3HT to study the electron transfer to metal oxides because the presence of fullerene to the blend films generally causes strong quenching of fluorescence making thus difficult to probe changes in the exciton lifetime with and without POM at the metal oxide/photoactive blend interfaces. In Figures 7a and c we show the steady-state photoluminescence (PL) spectra of the P3HT films deposited on TiO_2 and ZnO layers, respectively, with and without the POM modification. We observe the characteristic emission peaks of P3HT at around 650 and 720 nm corresponding to the 0-0 transition and the 0-1 and 0-2 sidebands.[53] The PL intensity of P3HT on metal oxides, especially on TiO_2, is significantly reduced upon POM coverage, which is an indication of the enhanced electron accepting capability of tBuSiOH-POM. Noteworthy is the reduction in the PL intensity of P3HT:$IC_{60}BA$ blend films on POM-modified substrates (Figure S15), indicating that tBuSiOH-POM successfully mediates electron transfer from P3HT to the TiO_2 and ZnO CB and its performance as an interfacial electron shuttle is not vanished in the presence of a strong electron acceptor such as $IC_{60}BA$.

Time-resolved photoluminescence (TRPL) measurements were carried out on P3HT films deposited on metal oxide and metal oxide/tBuSiOH-POM substrates to also elucidate the electron transfer mediating capability of POM by analyzing the exciton recombination dynamics at the metal oxide/POM/organic interfaces. Such emission studies only probe the excited state of P3HT, so faster electron transfer should increase emission decay rate. Figures 7b and d show the normalized transient PL decay curves obtained with a femtosecond laser of the P3HT/TiO_2 and P3HT/ZnO films, respectively, before and after POM interfacial modification. The excitation wavelength was set at 410 nm and emission wavelength at 700 nm, close to the maximum of the emission band of P3HT. We fitted the curves and obtained the corresponding decay lifetimes with a bi-exponential decay function except of the ZnO/tBuSiOH-POM/P3HT sample were a three-exponential function was applied (Table S3). In the case of TiO_2 substrate, the presence of tBuSiOH-POM dramatically accelerates the PL decay process with the average decay lifetime τ decreasing from 7.4 to 1.2 ps. This is consistent with the POM being an excellent electron acceptor/mediator to TiO_2.

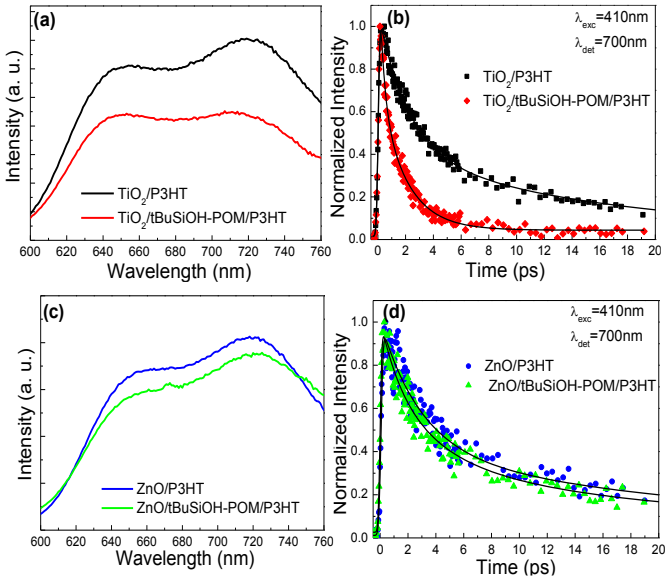

Figure 7 (a) Steady-state and (b) transient PL spectra of P3HT thin films on as-deposited and tBuSiOH-POM coated TiO_2 substrates. (c) Steady-state and (d) transient PL spectra of P3HT thin films on as-deposited and tBuSiOH-POM coated ZnO substrates.

However, although the POM coverage of TiO_2 granted a substantial quenching of the decay lifetime τ thus verifying the role of functionalized POM as electron acceptor and electron transfer mediator, it induced smaller deviation in the already higher exciton lifetime of P3HT on ZnO (from 10.3 to 9.0 ps) as compared to TiO_2. There are several factors responsible for the observed difference in steady state and transient PL spectra of P3HT on TiO_2 and ZnO. One, is the slower electron injection into ZnO than TiO_2 due to the smaller effective electron mass and, consequently, the lower density of acceptor states in ZnO.[65,66] If the electron injection rate into ZnO is slow enough to permit competition of internal deactivation of the excited P3HT, then the electron transfer yield from POM into ZnO decreases. A second factor is that bound charge-transfer pairs are formed, between electrons injected into the oxide CB and the positively charged P3HT species,[65] which suffer from fast recombination before full charge separation occurs, and thus the number of injected electrons in the oxide CB band decreases. This is more efficient in ZnO due to its lower dielectric constant as compared to TiO_2. POM modification restricts but not completely eliminates the formation of charge-transfer species. In addition, upon POM coating effective surface passivation of surface defect states, which are of higher density in ZnO as compared to TiO_2,[67] is expected to increase the effective exciton lifetime,[19,68] thus acting antagonistically with the reduction in exciton lifetime caused by effective electron transfer from the LUMO of P3HT to the metal oxide CB via the POM path.

Conclusions

In conclusion, high-efficiency inverted P3HT:$IC_{60}BA$-based polymer solar cells with an average PCE of 6.51% were fabricated with the insertion of a silanol-functionalized polyoxometalate layer in the electron collecting contact within the inverted device structure. The efficiency enhancement of the devices mainly originates from the large reduction in the W_F of TiO_2 and ZnO cathode interlayers and from the excellent electron transfer capability of tBuSiOH-POM to metal oxides. In addition, the passivation of metal oxides surfaces and the corresponding decrease in surface energy of metal oxide substrates via the anchoring of silanol groups which induced better nanomorphology of the photoactive blend also contributed to improved device performance. The modified devices exhibited significantly improved lifetime retaining 90% of their initial PCEs after air exposure for 1000 hours. This work obviates laborious synthesis of appropriately functionalized polyoxometalates as effective interlayers in high efficiency and air-stable solution-processed polymer solar cells and related devices.

Acknowledgements

A. S. acknowledges an IKY-fellowship and co-financed by the European Social Fund-ESF and Greek national funds under the "Strengthening Post-Doctoral Research (MIS: 5001552)" through the Operational Program "National Human Resources Development Program, Education and Lifelong Learning" (priority axes 6,8,9). Y. T. and M. K. acknowledge that part of this work also has been supported by TUBITAK 2211-C program and Selcuk University BAP office (PN:14201047). A.F. acknowledges postdoctoral funding from Alexander von Humboldt Foundation. T. P. acknowledges use of HPC computational facilities provided by the Faculty of Science and Engineering, University of Chester, U.K.

Bibliography

1. G. Yu, J. Hummelen, F. Wudl, A. J. Heeger, *Science*, 1995, **270**, 1789–1791.
2. Z. He, C. Zhong, S. Su, M. Xu, H. Wu, Y. Cao, *Nat. Photonics*, 2012, **6**, 591–595.
3. J. J. M. Halls, C. A. Walsh, N. C. Greenham, E. A. Marseglia, R. H. Friend, S. C. Moratti , A. B. Holmes, *Nature*, 1995, **376**, 498–500.
4. L. Dou, J. You, J. Yang, C.-C. Chen, Y. He, S. Murase, T. Moriarty, K. Emery, G. Li, Y. Yang, *Nat. Photonics*, 2012, **6**, 180–185.
5. J. You, L. Dou, K. Yoshimura, T. Kato, K. Ohya, T. Moriarty, K. Emery, C.-C. Chen, J. Gao, G. Li, Y. Yang, *Nat. Comm.*, 2013, 4, 1446.
6. Y. J. Cheng, S. H. Yang, C. S. Hsu, *Chem. Rev.*, 2009, **109**, 5868–5923.
7. Y. Y. Liang, L. P. Yu, *Acc. Chem. Res.*, 2010, **43**, 1227–1236.
8. Y. F. Li, *Acc. Chem. Res.*, 2012, **45**, 723–733.
9. J. Peet, J. Y. Kim, N. E. Coates, W. L. Ma, D. Moses, A. J. Heeger, G. C. Bazan, *Nat. Mater.*, 2007, **6**, 497–500.
10. G. Li, V. Shrotriya, J. Huang, Y. Yao, T. Moriarty, K. Emery, Y. Yang, *Nat. Mater.*, 2005, **4**, 864–868.
11. P. M. Beaujuge, J. M. J. Frechet, *J. Am. Chem. Soc.*, 2011, **133**, 20009–20029.
12. J. K. Lee, W. L. Ma, C. J. Brabec, J. Yuen, J. S. Moon, J. Y. Kim, K. Lee, G. C. Bazan, A. J. Heeger, *J. Am. Chem. Soc.*, 2008, **130**, 3619–3623.
13. M. Vasilopoulou, A. M Douvas, D. G. Georgiadou, V. Constantoudis, D. Davazoglou, S. Kennou, L. C. Palilis, D. Daphnomili, A. G. Coutsolelos, P. Argitis, *Nano Res.*, 2014, **7**, 679–693.
14. Y. M. Sun, J. H. Seo, C. J. Takacs, J. Seifter, A. J. Heeger, *Adv.Mater.*, 2011, **23**, 1679–1683.
15. S.-H. Liao, H.-J. Jhuo, Y.-S. Cheng, S.-A. Chen, *Adv. Mater.* 2013**, 25**, 4766–4771.
16. S. Chen, X. Du, G. Ye, J. Cao, H. Sun, Z. Xiao, L. Ding, *J. Mater. Chem. A* **2013**, *1*, 11170–11176.
17. S. Trost, K. Zilberberg, A. Behrendt, A. Polywka, P. Görrn, P. Reckers, J. Maibach, T. Mayer, T. Riedl, *Adv. Energy Mater.*, 2013, **3**, 1437–1444.
18. M. Prosa, M. Tessarolo, M. Bolognesi, O. Margeat, D. Gedefaw, M. Gaceur, C. Videlot Ackermann, M. R. Andersson, M. Muccini, M. Seri, J. Ackermann, *ACS Appl. Mater. Interfaces*, 2016, **8**, 1635–1643.
19. M. Vasilopoulou, D. G. Georgiadou, A. Soultati, N. Boukos, S. Gardelis, L. C. Palilis, M. Fakis, G. Skoulatakis, S. Kennou, M. Botzakaki, S. Georga, C. A. Krontiras, F. Auras, D. Fattakhova-Rohlfing, T. Bein, T. A. Papadopoulos, D. Davazoglou, P. Argitis, *Adv. Energy Mater.*, 2014, **4**, 1400214.
20. A. C. Papageorgiou, N. S. Beglitis, C. L. Pang, G. Teobaldi, G. Cabailh, Q. Chen, A. J. Fisher, W. A. Hofer, G. Thornton, *Proc. Natl. Acad. Sci. USA*, 2010, **107**, 2391–2396.
21. I. Lange, S. Reiter, M. Pätzel, A. Zykov, A. Nefedov, J. Hildebrandt, S. Hecht, S. Kowarik, C. Wöll, G. Heimel, D. Neher, *Adv. Funct. Mater.*, 2014, **24**, 7014–7024.

22. S. Bai, Y. Jin, X. Liang, Z. Ye, Z. Wu, B. Sun, Z. Ma, Z. Tang, J. Wang, U. Würfel, F. Gao, F. Zhang, *Adv. Energy Mater.* **2015**, *5*, 1401606.
23. S. B. Jo, J. H. Lee, M. Sim, M. Kim, J. H. Park, Y. S. Choi, Y. Kim, S.-G. Ihn, K. Cho, *Adv. Energy Mater.*, 2011, **1**, 690–698.
24. Z. Li, X. Zhang, C. Liu, Z. Zhang, J. Li, L. Shen, W. Guo, S. Ruan, *ACS Appl. Mater. Interfaces*, 2016, **8**, 8224–8231.
25. C. Sun, X. Li, G. Wang, P. Li, W. Zhang, T. Jiu, N. Jiang, J. Fang, *RSC Adv.*, 2014, **4**, 19529–19532.
26. D. Yang, P. Fu, F. Zhang, N. Wang, J. Zhang, C. Li, *J. Mater. Chem. A***,** 2014, **2**, 17281–17285.
27. S. W. Heo, T. H. Huong Le, T. Tanaka, I. Osaka, K. Takimiya, K. Tajima, *J. Mater. Chem. A***,** 2017, **5**, 10347–10354.
28. X. Lin, Y. Yang, L. Nian, H. Su, J. Ou, Z. Yuan, F. Xie, W. Hong, D. Yu, M. Zhang, Y. Mab, X. Chen, *Nano Energy*, 2016, **26**, 216–223.
29. S. Nam, J. Seo, S. Woo, W. H. Kim, D. D. C. Bradley, Y. Kim, *Nature Commun.*, 2015, **6**, 8929.
30. M. Thambidurai, J. Y. Kim, Y. Ko, H.-J. Song, H. Shin, J. Song, Y. Lee, N. Muthukumarasamy, D. Velauthapillaic, C. Lee, *Nanoscale*, 2014, **6**, 8585–8589.
31. S. Trost, T. Becker, A. Polywka, P. Görrn, M. F. Oszajca, N. A. Luechinger, D. Rogalla, M. Weidner, P. Reckers, T. Mayer, T. Riedl, *Adv. Energy Mater.*, 2016, **6**,1600347.
32. G. Kim, J. Kong, J. Kim, H. Kang, H. Back, H. Kim, K. Lee, *Adv. Energy Mater.*, 2015, **5**, 1401298.
33. T. Stubhan, I. Litzov, N. Li, M. Salinas, M. Steidl, G. Sauer, K. Forberich, G. J. Matt, M. Halik, C. J. Brabec, *J. Mater. Chem. A*, 2013, **1**, 6004–6009.
34. S. Trost, T. Becker, K. Zilberberg, A. Behrendt, A. Polywka, R. Heiderhoff, P. Görrn, T. Riedl, *Sci. Rep.*, 2015, **5,** 7765.
35. E. Polydorou, A. Zeniou, D. Tsikritzis, A. Soultati, I. Sakellis, S. Gardelis, T. A. Papadopoulos, J. Briscoe, L. C. Palilis, S. Kennou, E. Gogolides, P. Argitis, D. Davazoglou, M. Vasilopoulou, *J Mater. Chem. A*, 2016, **30**, 11844–11858.
36. E. Polydorou, I. Sakellis, A. Soultati, A. Kaltzoglou, T. A. Papadopoulos, J. Briscoe, D. Tsikritzis, M. Fakis, L. C. Palilis, S. Kennou, P. Argitis, P. Falaras, D. Davazoglou, M. Vasilopoulou, *Nano Energy*, 2017, **34**, 500–514.
37. J. M. Sumliner, H. Lv, J. Fielden, Y. V. Geletii, C. L. Hill, *Eur. J. Inorg. Chem.*, 2014, **4**, 635–644.
38. M. Vasilopoulou, I. Raptis, P. Argitis, I. Aspiotis, D. Davazoglou, *Microelectron. Eng., 2006,* **83**, 1414–1417.
39. L. C. Palilis, M. Vasilopoulou, D. G. Georgiadou, P. Argitis, *Org. Electron.*, 2010, **11**, 887–894.
40. L. C. Palilis, M. Vasilopoulou, A. M. Douvas, D. G. Georgiadou, S. Kennou, N. A. Sthathopoulos, V. Constantoudis, P. Argitis, *Sol. Energy Mater. Sol. Cells*, 2013, **114**, 205–213.
41. M. Vasilopoulou, A. M. Douvas, L.C. Palilis, S. Kennou, P. Argitis, *J. Am. Chem. Soc.*, 2015, **137**, 6844–6856.
42. Y. C. Chen, S. Wang, L. W. Xue, Z. G. Zhang, H. L. Li, L. X. Wu, Y. Wang, F. H. Li, F. L. Zhang, Y. F. Li, *J. Mater. Chem. A*, 2016, **4**, 19189–19196.
43. Y. Chen, S. Zhang, Q. Peng, L. Wu, F. Li, Y. Wang, *J. Mater. Chem. A*, 2017, **5**, 15294–15301.
44. M. Tountas, Y. Topal, E. Polydorou, A. Soultati, A. Verykios, A. Kaltzoglou, T. A. Papadopoulos, F. Auras, K. Seintis, M. Fakis, L. C. Palilis, D. Tsikritzis, S. Kennou, M. Koutsoureli, G. Papaioannou, M. Ersöz, M. Kus, P. Falaras, D. Davazoglou, P. Argitis, M. Vasilopoulou, *ACS Appl. Mater. Interfaces*, 2017, **9**, 22773–22787.
45. E. Galoppini, *Coord. Chem. Rev.*, 2004, **248**, 1283–1297.
46. A. M. Love, C. A. Carrero, A. Chieregato, J. T. Grant, S. Conrad, R. Verel, I. Hermans, *Chem. Mater.*, 2016, **28**, 5495–5504.
47. A. Mazeaud, N. Ammani, F.Robert, R. Thovenot, *Angew. Chem., Int. Ed. Engl.*, 1996, **35**, 1961–1964.
48. D. Zhang, K. Wang, Q. Yan, P. Ma, and J. Wang, *Chinese J. Inorg. Chem*., 2012, **10**, 2236-2240.
49. A. Walsh, K. T. Butler, *Acc. Chem. Res.*, 2014, **47**, 364–372.
50. G. Zhao, Y. He, Y. Li, *Adv. Mater.*, 2010, **22**, 4355–4358.
51. K. D. Kim, D. C. Lim, J. Hu, J. D. Kwon, M. G. Jeong, H. O. Seo, J. Y. Lee, K. Y. Jang, J. H. Lim, K. H. Lee, Y. Jeong, Y. D. Kim, S. Cho, *ACS Appl. Mater. Interfaces*, 2013, **5**, 8718–8723.
52. S. A. Hawks, F. Deledalle, J. Yao, D. G. Rebois, G. Li, J. Nelson, Y. Yang, T. Kirchartz, J. R. Durrant, *Adv. Energy Mater.*, 2013, **3**, 1201–1209.
53. M. A. Ruderer, S. Guo, R. Meier, H.-Y. Chiang, V. Körstgens, J. Wiedersich, J. Perlich, S. V. Roth, P. Müller-Buschbaum, *Adv. Funct. Mater.*, 2011, **21**, 3382–3391.
54. M. Sunderberg , O. Inganäs, S. Stafström, G. Gustafsson , B. Sjögren, *Solid State Commun.*, 1989, **71**, 435–439.
55. E. Zimmermann, P. Ehrenreich, T. Pfadler, J. A. Dorman, J. Weickert, L. Schmidt-Mende, *Nat. Photonics*, 2014, **8**, 669–672.
56. S. R. Cowan, R. A. Street, S. Cho and A. J. Heeger, *Phys. Rev. B: Condens. Matter Mater. Phys.*, 2011, **83**, 035205.
57. Q. Zhang, B. Kan, F. Liu, G. K. Long, X. J. Wan, X. Q. Chen, Y. Zuo, W. Ni, H. J. Zhang, M. M. Li, Z. C. Hu, F. Huang, Y. Cao, Z. Q. Liang, M. T. Zhang, T. P. Russell, Y. S. Chen, *Nat. Photonics*, 2015, **9**, 35–41.
58. L. Reinhardt, M. Grein, C. Bühler, M. Schubert, U. Würfel, *Adv. Energy Mater.*, 2014, ***5***, 1400081.
59. U. Würfel, D. Neher, A. Spies, S. Albrecht, *Nat Commun.*, 2015, **6**, 6951.
60. M. C. Scharber, *Adv. Mater.*, 2016, **28**, 1994–2001.
61. E. Ngo, S. Venkatesan, D. Khatiwada, C. Zhang, Q. Qiao, *ACS Appl. Mater. Interfaces*, 2015, **7**, 16093–16100.
62. J. Zhu, M. Vasilopoulou, D. Davazoglou, S. Kennou, A. Chroneos, U. Schwingenschlögl, *Sci. Rep.*, 2017, **7**, 40882.
63. X. Bulliard , S.-G. Ihn , S. Yun , Y. Kim , D. Choi , J.-Y. Choi, M. Kim, M. Sim, J.-H. Park, W. Choi, K. Cho, *Adv. Funct. Mater.*, 2010, **20**, 4381–4387.
64. S. B. Ambade, R. B. Ambade, S. S. Bagde, S.-H. Lee, *ACS Appl. Mater. Interfaces*, 2016, **8**, 35270–35280.
65. C. Martín, M. Ziołek, M. Marchena, A. Douhal, *J. Phys. Chem. C*, 2011, **115**, 23183−23191.
66. J. Sobus, G. Burdzinski, J. Karolczak, J. Idígoras, J. A. Anta, M. Ziołek, *Langmuir*, 2014, **30**, 2505−2512.
67. A. M. Ali, E. A. C. Emanuelsson, D. A. Patterson, *Appl. Catal. B: Environmental*, 2010, **97**, 168–181.
68. W. Li, W. Zhang, S. Van Reenen, R. J. Sutton, J. Fan, A. A. Haghighirad, M. B. Johnston, L. Wang, H. J. Snaith, *Energy Environ. Sci.*, 2016, **9**, 490–498.